



ELSEVIER

Available online at [www.sciencedirect.com](http://www.sciencedirect.com)

SCIENCE @ DIRECT®

Nuclear Instruments and Methods in Physics Research A 538 (2005) 159–177

NUCLEAR  
INSTRUMENTS  
& METHODS  
IN PHYSICS  
RESEARCH  
Section A

[www.elsevier.com/locate/nima](http://www.elsevier.com/locate/nima)

# Muon acceleration in FFAG rings

E. Keil<sup>a,\*</sup>, A.M. Sessler<sup>b</sup>

<sup>a</sup>*CERN, CH-1211 Geneva 23, Switzerland*

<sup>b</sup>*Lawrence Berkeley National Laboratory, Berkeley, CA, USA*

Received 1 July 2004; received in revised form 30 August 2004; accepted 31 August 2004

Available online 3 November 2004

## Abstract

Muon acceleration from 6 or 10 to 20 GeV in fixed-field alternating gradient (FFAG) rings is considered. The novel physics issues associated with non-scaling FFAG machines, namely the very acceleration process and the crossing of transverse imperfection resonances are addressed. These FFAG machines are essentially strong-focusing rings with a dispersion small enough to keep muons over the full momentum range inside the same magnet aperture. We consider two cases: (i) A Modified FODO Ring with about a metre long straight sections, enough to house normal-conducting RF cavities at about 200 MHz and (ii) A Doublet Ring with a few metres long straight sections, enough for superconducting RF cavities also at about 200 MHz. Parameters are derived for the lattice and RF system of an electron model. It accelerates electrons from about 10–20 MeV and allows one to study the critical issues of non-scaling FFAGs. For both a full machine and a model, lattice parameters such as magnet type and dimension, spacing, and number of cells are presented. The consequences of misaligned magnets are studied by simulation. Practical RF system design issues, e.g. RF power, and the limit on the bunch population due to beam loading are estimated.

© 2004 Elsevier B.V. All rights reserved.

PACS: 29.20.Mr; 29.27.Eg; 41.75.Ak

Keywords: FFAG accelerator; Muons

## 1. Introduction

Recently, fixed-field alternating gradients (FFAGs) have received considerable attention as devices to be employed for the acceleration of

muons [1–8] in neutrino factories. Prior to these studies, neutrino factory studies [9–11], based on accelerating and storing muons, had assumed that the muons are accelerated in a linear accelerator up to a few GeV, and in one or two recirculating linear accelerators (RLA) similar to the Continuous Electron Beam Accelerator Facility (CEBAF) at the Thomas Jefferson National Accelerator Facility to the energy of the storage

\*Corresponding author. +49 30 8940 8139; fax: +49 30 8940 8142.

E-mail address: [Eberhard.Keil@t-online.de](mailto:Eberhard.Keil@t-online.de) (E. Keil).

ring, in the range of 20–50 GeV. In an RLA, the muons travel through two linear accelerators several times, and through half-circular arcs, one for each recirculation, at either end. Between the linear accelerators and the arcs are spreaders, which distribute the muons of different energy from the linear accelerators into the arcs, and combiners, which do the opposite. Spreaders and combiners become rapidly more complicated and costly when the number of recirculations increases; it is 4 or 5 in Refs. [9–11].

FFAG rings are an alternative to recirculating linear accelerators. Muons are accelerated by a factor between 2 and 3 in a lattice with a single aperture. There are no spreaders and combiners. Such rings hold the promise of a larger number of recirculations, and hence of reduced cost. There are two varieties of FFAG rings: scaling and non-scaling. In scaling FFAG rings, which are predominantly studied in Japan [1], the parameters of the elements are adjusted such that the tunes  $Q_x$  and  $Q_y$  are constant over the whole radial aperture and momentum range. Non-scaling FFAG rings, which are predominantly studied in Europe and North America [3–8,12,13], have lattices that are essentially alternating-gradient lattices with focusing strong enough to achieve a small enough dispersion and spread in flight time over the whole momentum range. The tunes  $Q_x$  and  $Q_y$  in such rings straddle many integral and half-integral resonances.

In this paper we extend the previous work on non-scaling FFAGs. First we present, in Section 2, a discussion of the novel physics issues associated with non-scaling FFAGs. We then discuss, in Section 3, the development of two new lattices, and the careful consideration of aspects of these two lattices required in real machines. We then, in Section 4, extend earlier work [14,15], and consider an electron model that would allow one to experimentally study the novel aspects of non-scaling FFAGs. The lattice parameters for this model are derived from those circulated by Berg [16] at the FFAG Workshop, held from 13 to 17 October 2003 at BNL. Our conclusions are presented in Section 5. We do not consider, in this paper, injection and extraction, diagnostics, and magnet design.

## 2. Accelerator physics issues

There are two major physics issues associated with the use of FFAGs for muon acceleration. The first is associated with acceleration. The acceleration must be fast (compared to a muon decay time) and that precludes acceleration in the normal manner; namely acceleration by putting the particles inside an RF bucket and adiabatically changing the bucket parameters. For muons, as was first realised by Berg [17,18] and Johnstone and Koscielniak [5,19], the acceleration must be outside buckets. We explore the restrictions this imposes in Section 2.1.

The second major issue is that in non-scaling FFAGs, which we employ as they have many advantages over scaling FFAGs, it is inevitable that in the course of acceleration transverse resonances are crossed. However, the crossing is fast, and most resonances can be traversed without particle loss. In particular, we find that this is true, if the alignment tolerance is in the range, depending on the lattice, between 0.03 and 0.1 mm. We study the restrictions imposed by resonance crossing in Section 2.2.

### 2.1. Acceleration

The particle motion in longitudinal phase space can be understood by inspecting the longitudinal Hamiltonian  $H_1$  in the variables phase,  $\varphi$ , measured in cycles, and momentum error,  $p_t$ , relative to the reference momentum  $p_r$  [20]:

$$H_1(p_t, \varphi) = \frac{2\pi h \beta_r^2 E_r}{e V N_c} \left( \frac{\eta_0 p_t^2}{2} + \frac{\eta_1 p_t^3}{3} + \frac{\eta_2 p_t^4}{4} + \dots \right) + [\cos 2\pi(\varphi_s + \varphi) + 2\pi\varphi \sin 2\pi\varphi_s - \cos 2\pi\varphi_s]. \quad (1)$$

Here,  $h$  is the harmonic number,  $V$  is the accelerating RF voltage in one of  $N_c$  cavities,  $\varphi_s$  is the stable phase angle, also measured in cycles and counted from the last zero crossing of the RF wave form, and  $\beta_r$  and  $E_r$  are the speed in units of the light velocity, and energy of the reference particle. The origin of  $\varphi$  is at the stable phase angle  $\varphi_s$ . The coefficients  $\eta_i$  are the slip factor  $\eta_0$  and its higher order terms.

2.1.1. Linear longitudinal motion

The usual analysis neglects all slip factors except  $\eta_0$ , assumes stationary buckets with  $\varphi_s = 1/2$ , and introduces the scaled momentum variable  $y$ :

$$y = p_t \left( \frac{\pi h \beta_r^2 E_r \eta_0}{2eVN_c} \right)^{1/2} = \frac{p_t}{p_b}. \quad (2)$$

The coefficient of  $p_t$  in Eq. (2) can be identified as the inverse half height  $p_b$  of the stationary bucket. In terms of  $y$  and  $\varphi$ , the Hamiltonian becomes simply

$$H_2(y, \varphi) = y^2 + \sin^2 \pi \varphi. \quad (3)$$

Fig. 1 shows a contour plot of the Hamiltonian  $H_2$ , and confirms that  $y = 1$  indeed corresponds to the half bucket height. The stable fixed point is at  $\varphi = y = 0$ . Unstable fixed points are at  $\varphi = \pm 1/2$  and  $y = 0$ .

2.1.2. Longitudinal motion with quadratic and cubic terms

When considering non-scaling FFAG rings we must include in the Hamiltonian a term in  $y^3$  with coefficient  $a = \eta_1 p_b / \eta_0$  that takes care of the

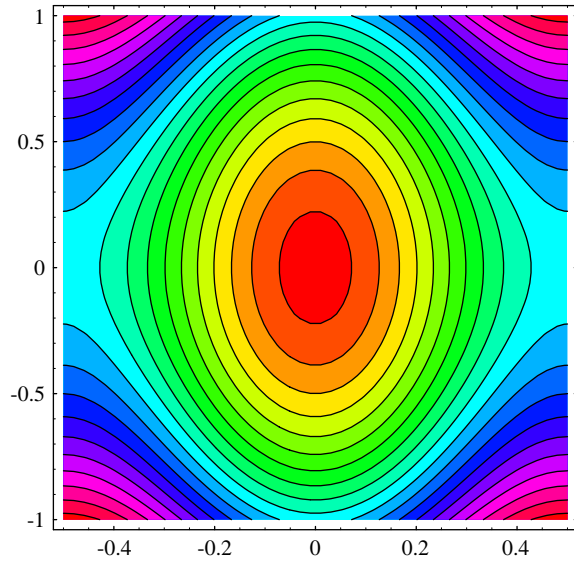


Fig. 1. Contour plot of Hamiltonian  $H_2$  for linear motion. Muons move along level lines. The largest swing in energy is given by the largest elliptical band. The abscissa is phase  $\varphi$ , the ordinate is scaled energy, cf. Eq. (2).

quadratic variation of the travel time with the relative momentum error  $p_t$ , and write

$$H_3(y, \varphi, a) = y^2 + \frac{2a}{3} y^3 + \sin^2 \pi \varphi. \quad (4)$$

Fig. 2 shows a contour plot of the Hamiltonian  $H_3$  for  $a = 1$ . At  $y = -1/a$ , new stable and unstable fixed points alternate at  $\varphi = \pm 1/2$  and  $\varphi = 0$ . They occur at  $y = -1/a$ , because the travel time  $\partial H_3 / \partial y = 2y(1 + ay)$  has a second zero there. Acceleration in non-scaling FFAG rings usually employs motion along the  $\Omega$ -shaped trajectories, which start below the fixed point at  $\varphi = \pm 1/2$  and  $y = -1/a$ , circle around the fixed point at  $\varphi = 0$  and  $y = 0$ , and reach the maximum  $y$  above it. This is the case in the FODO lattice described in Section 3.1.

We study the separatrices in order to find the limit on  $a$  for the  $\Omega$ -shaped trajectories. It is known that the separatrices pass through the unstable fixed points. The two types of unstable fixed points correspond to two types of separatrices, when  $a \neq 0$ . We find them by solving two equations for  $y$ :

$$H_3(\varphi, y, a) = H_3(-1/2, 0, a), \quad (5)$$

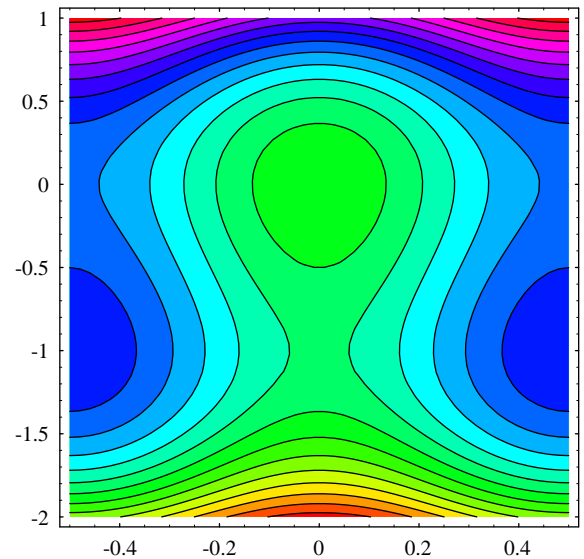


Fig. 2. Contour plot of Hamiltonian  $H_3$  at  $a = 1$ . Acceleration along  $\Omega$ -shaped trajectories. The abscissa is phase  $\varphi$ , the ordinate is scaled energy, cf. Eq. (2).

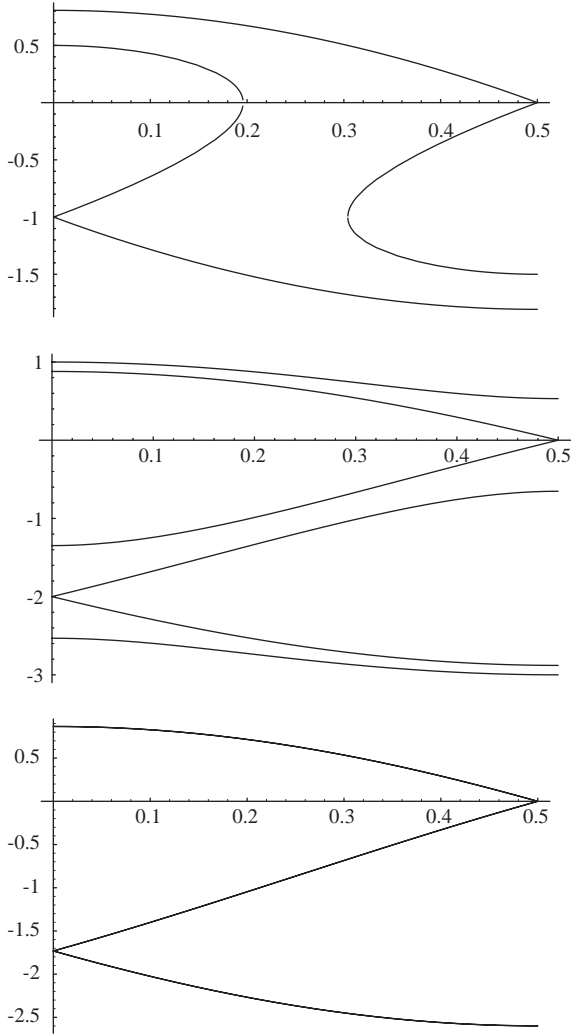


Fig. 3. Separatrices of the Hamiltonian  $H_3$  in Eq. (4) at  $a = 1$  on the top, at  $a = 1/2$  in the middle, and at  $a = 1/\sqrt{3}$  on the bottom.

$$H_3(\varphi, y, a) = H_3(0, -1/a, a). \quad (6)$$

Fig. 3 show the separatrices for three values of  $a$ , using symmetry and plotting only for  $0 \leq \varphi \leq 1/2$ . At  $a = 1$ , particles are accelerated along trajectories in the S-shaped channel between islands, which starts between the separatrices in the lower right corner below  $y = -3/2a$ , and ends between the separatrices in the upper left corner

above  $y = 1/2a$ . At  $a = 1/2$ , the regular bucket centred at  $\varphi = y = 0$  blocks acceleration across  $y = 0$ . At  $a = 1/\sqrt{3}$ , the buckets centred at  $\varphi = y = 0$  and at  $\varphi = 1/2$  and  $y = -\sqrt{3}$  just touch, and the channel of acceleration has width zero, in agreement with Ng's result [20]. The half height of the bucket at the threshold is  $p_{\text{th}} = \eta_0/\eta_1\sqrt{3}$ . The peak accelerating voltage of the RF cavities follows from Eq. (2).

### 2.1.3. Longitudinal motion near transition

Muon acceleration rings and electron models are often operated with the reference energy equal to the transition energy, and  $\eta_0 = 0$ . Ignoring the terms proportional to  $\eta_i$  with  $i \geq 2$  in Eq. (1), the new Hamiltonian  $H_4$  becomes much simpler:

$$H_4(p_t, \varphi) = \frac{2\pi\beta_r^2 E_r h \eta_1 p_t^3}{3eVN_c} + [\cos 2\pi(\varphi_s + \varphi) + 2\pi\varphi \sin 2\pi\varphi_s - \cos 2\pi\varphi_s]. \quad (7)$$

The first term may be taken as the cube of a scaled momentum variable  $y$ :

$$y = p_t \left( \frac{2\pi\beta_r^2 E_r h \eta_1}{3eVN_c} \right)^{1/3}. \quad (8)$$

In the scaled variables  $y$  and  $\varphi$ , the Hamiltonian  $H_5(y, \varphi)$  becomes, assuming stationary buckets with  $\varphi_s = 1/2$  as before:

$$H_5(y, \varphi) = y^3 + \sin^2 \pi\varphi. \quad (9)$$

Fig. 4 shows a contour plot of  $H_5(y, \varphi)$ . Acceleration along the bright band has the property that initial and final  $y$  have the same magnitude  $|y| = 1$  and opposite sign, as is appropriate for accelerating muons from 10 to 20 GeV at 15 GeV reference energy in the Doublet Lattice described in Section 3, or electrons from 10 to 20 MeV at 15 MeV reference energy in the electron model described in Section 4. These ranges correspond to accelerating from  $p_t = -1/3$  to  $p_t = +1/3$ . Solving Eq. (8) with  $|y| = 1$  for  $p_t$  yields the acceleration range for given parameters:

$$p_t = \left( \frac{3eVN_c}{2\pi\beta_r^2 E_r h \eta_1} \right)^{1/3}. \quad (10)$$

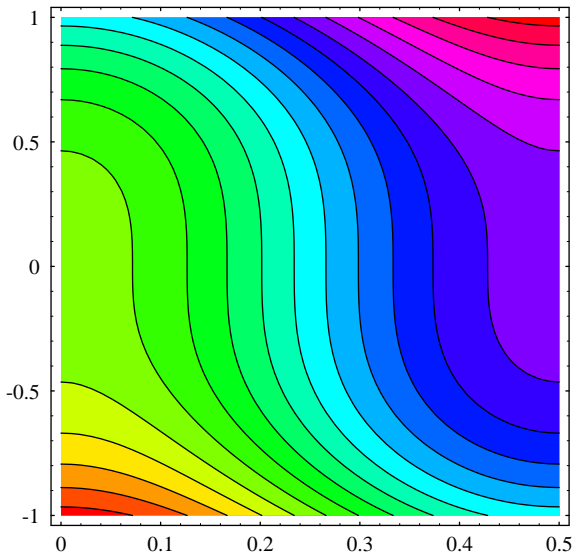


Fig. 4. Contour plot of the longitudinal Hamiltonian  $H_5(y, \varphi)$  in Eq. (9). The phases  $\varphi_s = 1/2$  and  $\varphi$  are measured in cycles. The abscissa is  $\varphi$ . The ordinate is the scaled momentum variable  $y$  (8).  $H_5$  is symmetrical around  $\varphi = 0$  and has period one in  $\varphi$ .

## 2.2. Resonance crossing

The phase advances  $\mu_x$  and  $\mu_y$  in a cell vary approximately in inverse proportion to the particle momentum. They should remain below the intrinsic half-integral resonance at the lower edge of the operating range in  $\delta p/p$ . In the whole FFAG ring with tens to hundreds of cells, the tunes  $Q_x$  and  $Q_y$  vary by tens to hundreds of units, while particles are accelerated through the operating range. Alignment and excitation errors of the elements drive integral and half-integral stop bands, which must be crossed during acceleration, but because the acceleration is fast these resonances are not deleterious. We shall study the crossing of error-driven resonances by simulation in Sections 3.4 and 4.4, once we have developed the lattices.

## 3. FFAG rings for muon acceleration

Some insight into the FFAG ring design can be gained by looking at scaling laws. An FFAG ring

for accelerating muons consists of  $N$  periods. Each period has length  $L$ . There are various lattice styles, i.e. arrangements of magnets. The FFAG ring should be designed such that the combination of parameters satisfies the conditions in Eqs. (2) and (10). Ng [21] gives closed expressions for  $\eta_0$  and  $\eta_1$  in a model FODO lattice with arbitrary phase advance and arbitrary  $N$ . For  $N \gg 1$ , the slip factors  $\eta_0$  and  $\eta_1$  are both independent of  $L$ , proportional to  $1/Q^2$ , and hence proportional to  $1/N^2$  at given phase advance. We verified numerically that the same holds for the lattice styles under consideration, and that the proportionality constant is of order unity. The circumference  $C$  and the harmonic number  $h$  at fixed RF frequency are proportional to the product  $LN$ . Assuming that the number of RF cavities  $N_c \propto N$ , it follows from Eq. (10), that the peak RF voltage  $V \propto L/N^2$ , while the total circumferential RF voltage  $N_c V \propto L/N$ . With  $C$  and ring cost proportional to  $LN$  and RF voltage and cost of the RF installation proportional to  $L/N$ , there is an optimum value of  $N$ , when the two cost components are equal. Various lattices of non-scaling FFAG rings for accelerating muons have already been proposed [3–8,12,13]. Below, we develop lattices of two types.

### 3.1. FFAG muon accelerator lattices

The first type is called ‘‘Modified FODO’’. It has 1.4 m long straight sections, long enough for a single-cell room-temperature RF cavity at about 200 MHz. For this purpose we employ a Modified FODO lattice, derived from Ref. [6] by halving the length of the lattice cell. Horizontal focusing happens in the quadrupole, while bending and vertical focusing happen in a combined-function dipole magnet. Table 1 shows parameters, Fig. 5 layout and optical functions. Fig. 6 shows the variation of the tunes  $Q_x$  and  $Q_y$  on the left, and the variation of the path length  $\delta(s)$  and travel time  $ct$  on the right in the Modified FODO lattice with the relative momentum error  $\delta p/p$ . The lower limit of the operating range in  $\delta p/p$  is caused by the steep rise of  $Q_x$  and  $Q_y$ , when the phase advances in a period approach one half from below. Two different calculations with MAD [22] yield  $\delta(s)$  and

*ct*. The TWISS command provides the results labelled  $\delta(s)$ , which is probably the difference in the path length between an off-momentum orbit and the reference orbit. Tracking with the TRACK command, starting on the off-momentum closed orbit, yields *ct*, which is probably the difference in flight time between the off-momentum and the reference particle, multiplied by the speed of light *c*. The differences between  $\delta(s)$  and *ct*, although small, indicate that the MAD [22] calculation is not highly accurate. Fitting a parabola to *ct* in the neighbourhood of  $\delta p/p = 0$  yields the slip factors  $\eta_0$  and  $\eta_1$  listed in Table 1. The second zeroes of  $\delta(s)$  and *ct* are at  $-0.473 < \delta p/p < -0.468$ ; and at  $-0.429 < \delta p/p < -0.423$ , respectively. Hence the Modified FODO lattice can accelerate from 6 to 20 GeV.

Table 1

Parameters of the modified FODO and doublet lattices for muons

	FODO	Doublet
Total reference energy <i>E</i> (GeV)	16	15
Energy range (GeV)	6...20	10...20
Range of $\delta p/p$	−.625...+.250	−.333...+.333
Range of hor. offsets in F magnets <i>x</i> (mm)	−62...69	−25...69
Period length <i>L<sub>p</sub></i> (m)	3.7	4.0
Number of periods <i>N<sub>p</sub></i>	280	100
Circumference <i>C</i> (m)	1036	400
Max. $\beta$ -functions $\beta_x/\beta_y$ (m)	8.17/7.74	5.84/5.87
Max. dispersion <i>D<sub>x</sub></i> (m)	0.220	0.133
Phase advances $\mu_x/\mu_y$	0.1/0.1	0.203/0.203
Chromaticities $\mu'_x/\mu'_y$	−.105/−.103	−.238/−.240
Magnetic gradients <i>G<sub>F</sub>/G<sub>D</sub></i> (T/m)	48.6/−38.9	52.6/−52.9
Dipole field <i>B<sub>F</sub>/B<sub>D</sub></i> (T)	0.0/2.4	−2.39/6.88
Path length spread (mm)	364	221
Slip factor $\eta_0$	0.000908	0.0
Slip factor $\eta_1$	0.002068	0.004233
RF frequency (MHz)	199.7	202.4
Number of RF cavities <i>N<sub>c</sub></i>	560	100
Peak RF cavity accel. voltage <i>V</i> (MV)	3.0	13.5
Circumferential accel. voltage <i>N<sub>c</sub>V</i> (MV)	1740	1350
Typical number of turns	11	9

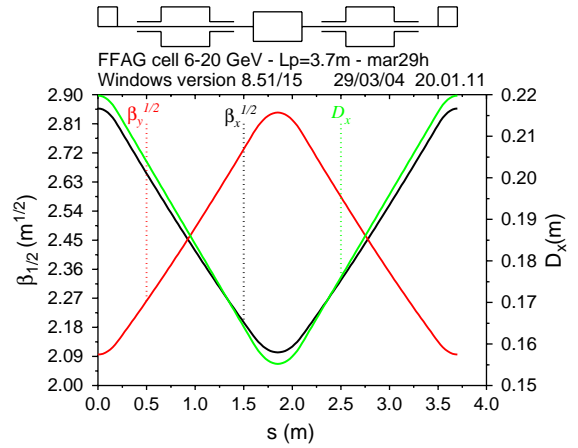


Fig. 5. Layout and optical functions of a cell in the Modified FODO lattice.

The second type is called “Doublet Lattice”. It has straight sections long enough, about 2 m, for one super-conducting single-cell RF cavity, per period, at about 200 MHz. Doublets of combined-function magnets between the RF cavities focus and bend the muon beam. The gradient of the magnets are adjusted such that the phase advance in a cell is  $q_x \approx q_y \approx 0.203$ . The bending angles are chosen such that the slip factor  $\eta_0$  vanishes at the reference energy, about 15 GeV. Table 1 shows parameters, Fig. 7 layout and optical functions. Fig. 8 shows the variation of the tunes  $Q_x$  and  $Q_y$ , on the left, and the variation of the path length  $\delta(s)$  and travel time *ct* on the right in the Doublet Lattice with the relative momentum error  $\delta p/p$ . The lower limit of the operating range in  $\delta p/p$  is caused by the steep rise of  $Q_x$  and  $Q_y$ , when the phase advances in a period approach one half from below. Fitting a parabola to *ct* in the neighbourhood of  $\delta p/p = 0$  yields the slip factors  $\eta_0$  and  $\eta_1$  listed in Table 1. Hence the Doublet Lattice can accelerate from about 10 GeV to about 20 GeV.

### 3.2. Practical lattice considerations

MAD [22] easily provides the maxima of the absolute value of the orbit offset  $|x_c|$ , and of the  $\beta$ -functions  $\beta_x^{\max}$  and  $\beta_y^{\max}$  as functions of the relative momentum error  $\delta p/p$ . We use them to

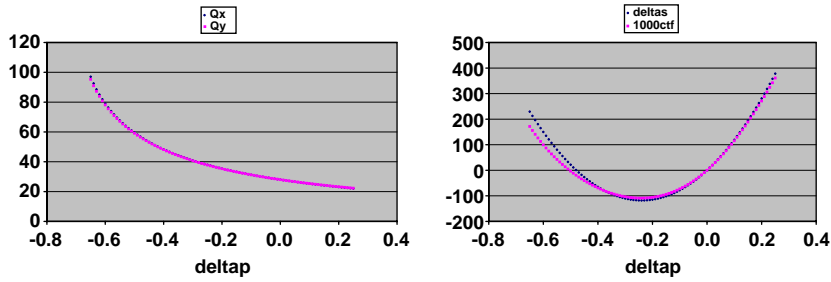


Fig. 6. Variation of the tunes  $Q_x$  and  $Q_y$  on the left, of the path length  $\delta(s)$  and travel time  $ct$  in mm on the right in the Modified FODO ring with the relative momentum error  $\delta p/p$ .

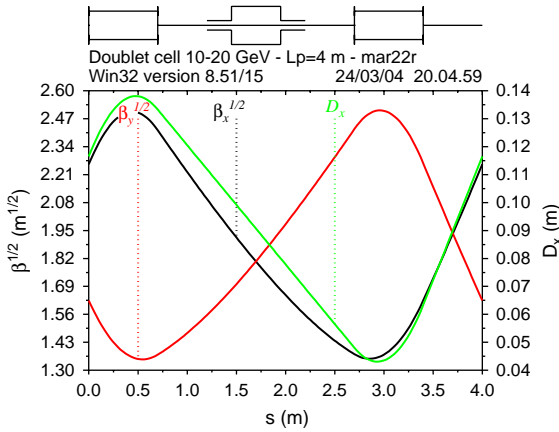


Fig. 7. Layout and optical functions of a cell in the Doublet Lattice.

compute the half apertures  $A_x$  and  $A_y$ . To find the contribution of the betatron oscillations to the aperture, we assume that the muon beam has a normalised RMS emittance  $\epsilon_n = 10/3$  mm, and allow for 3 RMS beam radii in the half aperture. We define  $\epsilon_n$  as the product of the RMS beam radius  $\sigma$  and RMS momentum spread  $\Delta p/p_r$ , in units of the muon rest momentum  $p_0$ . In the horizontal plane, we add the betatron beam size to the orbit offset  $|x_c|$ . Fig. 9 shows the half apertures  $A_x$  and  $A_y$  thus obtained as functions of the relative momentum error  $\delta p/p$ , for both the Modified FODO and the Doublet Lattice. In either lattice, a vertical aperture radius  $A_y \approx 50$  mm and a horizontal aperture radius  $A_x \approx 100$  mm are needed. Our method of combining the maximum values of orbit offset  $|x_c|$  and

$\beta$ -functions  $\beta_x^{\max}$  and  $\beta_y^{\max}$  surely overestimates the vertical aperture  $A_y$  of the F magnets and the horizontal aperture  $A_x$  of the D magnets. It also overestimates the magnetic field at the edge of the aperture in the D magnets.

### 3.3. Effects of misalignments on slowly accelerated beams

We start the study of the effects of misalignments by considering beams that are accelerated slowly, or not at all. We include the range of momenta between injection and ejection, and the associated horizontal and vertical tunes, straddling many integral resonances. However, in the applications to muon acceleration the beams are accelerated rapidly. We shall study the effects of misalignments on such beams in Section 3.4.2.

In the study of the effects of misalignments on a beam circulating at constant momentum in the Modified FODO lattice we were initially discouraged by the results of trials of random displacements of the magnets with a standard deviation of 0.1 mm. Hence, we were forced to adopt a standard deviation of 0.03 mm, which is tighter, by about a factor of three, than that achieved in existing machines. The distribution of the displacements is a Gaussian, truncated at 2.5 standard deviations. Fig. 10 shows the maxima of the absolute values of the horizontal and vertical orbit offset  $x_{co}^{\max}$  and  $y_{co}^{\max}$  in the Modified FODO ring due to the individual misalignment of all 560 magnets as a function of the horizontal tune  $Q_x$  and vertical tune  $Q_y$ . Here,  $y_{co}^{\max}$  is printed by MAD. We obtain  $x_{co}^{\max}$  from the value printed by

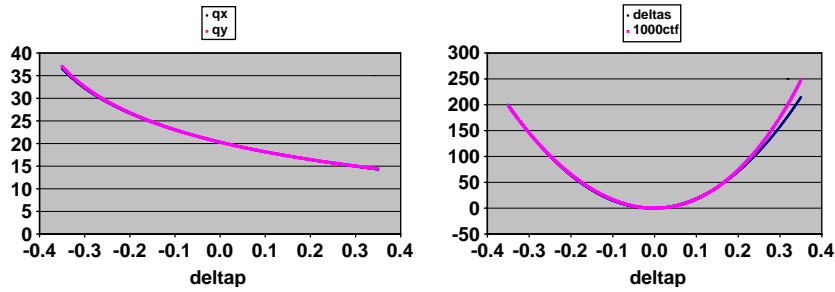


Fig. 8. Variation of the tunes  $Q_x$  and  $Q_y$  on the left, of the path length  $\delta(s)$  and travel time  $ct$  in mm on the right in the Doublet Lattice ring with the relative momentum error  $\delta p/p$ .

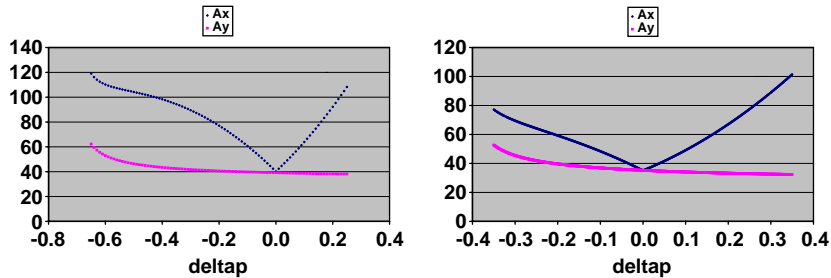


Fig. 9. Horizontal and vertical half apertures  $A_x$  and  $A_y$  of the Modified FODO and the Doublet Lattice in mm as functions of the relative momentum error  $\delta p/p$ .

MAD by subtracting the maximum absolute value of the horizontal orbit offset in the perfect machine, in order to remove the contribution of the dispersion  $D_x$  and  $\delta p/p$ . The spikes in  $x_{co}^{\max}$  and  $y_{co}^{\max}$  occur when the corresponding tunes  $Q_x$  or  $Q_y$  are close to an integer.

For the orbits of the reference particle at  $\delta p/p = 0$  due to the misalignment of all 560 individual magnets in 300 Modified FODO rings with different sets of displacements, we find  $\bar{x}_{co}^{\max} = 1.95 \pm 0.62$  mm and  $\bar{y}_{co}^{\max} = 1.93 \pm 0.63$  mm. In order to move the tunes at  $\delta p/p = 0$  to  $Q_x = 28.2$  and  $Q_y = 28.2$ , the phase advances are increased by 0.7%. We also find for the maximum absolute values of horizontal and vertical dispersion  $\bar{D}_x = 403 \pm 90$  mm and  $\bar{D}_y = 186 \pm 86$  mm. The mean value of  $D_x$  is about 83% larger than the design value. The strong excitation of the dispersion by misalignments is typical for lattices in

which the chromaticity is not corrected, as in all the lattices considered here [23–25].

In the Doublet Lattice, we assume that the RMS displacement of the individual magnets is 0.1 mm. Fig. 11 shows the maxima of the absolute values of the horizontal and vertical orbit offset  $x_{co}^{\max}$  and  $y_{co}^{\max}$  in the Doublet ring due to the individual misalignment of all 200 magnets as a function of the horizontal tune  $Q_x$  and vertical tune  $Q_y$ . For the orbits of the reference particle at  $\delta p/p = 0$  due to the misalignment of all 200 individual magnets in 300 Doublet rings with different sets of displacements, we find  $\bar{x}_{co}^{\max} = 4.11 \pm 1.22$  mm and  $\bar{y}_{co}^{\max} = 4.35 \pm 1.37$  mm, and  $\bar{D}_x = 332 \pm 88$  mm and  $\bar{D}_y = 225 \pm 101$  mm. The mean value of  $D_x$  is about a factor of 2.5 larger than the design value. In the Doublet Lattice, the orbit distortions, and the dispersion, in particular  $D_y$ , are larger than those in the Modified FODO lattice, as one

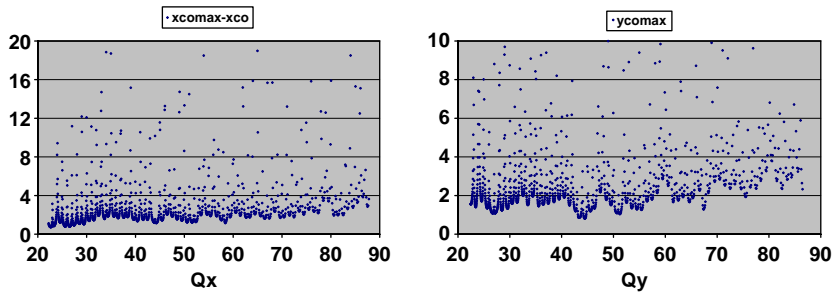


Fig. 10. Maxima of the absolute values of the horizontal and vertical orbit offset  $x_{\text{co}}^{\text{max}}$  and  $y_{\text{co}}^{\text{max}}$  in mm due to the misalignment as functions of the horizontal tune  $Q_x$  and vertical tune  $Q_y$ , respectively. All 560 magnets of the Modified FODO lattice are displaced individually.

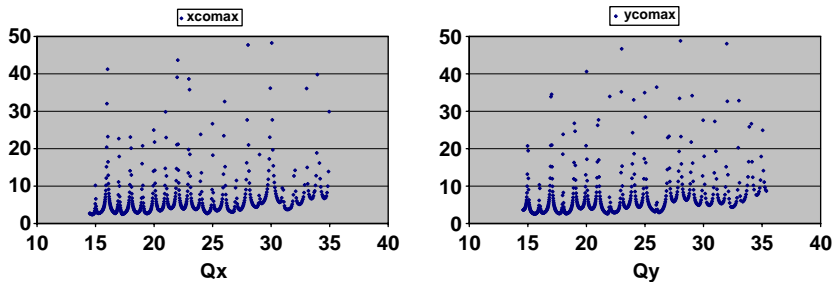


Fig. 11. Maxima of the absolute values of the horizontal and vertical orbit offset  $x_{\text{co}}^{\text{max}}$  and  $y_{\text{co}}^{\text{max}}$  in mm due to the misalignment as functions of the horizontal tune  $Q_x$  and vertical tune  $Q_y$ , respectively. All 200 magnets of the Doublet Lattice are displaced individually.

would expect because of the larger RMS displacements.

### 3.4. Acceleration in FFAG rings for muons

We study the acceleration in FFAG rings for muons by simulation in longitudinal phase space ( $ct, p_l = \Delta p/p_x$ ). The discussion in Section 2.1 and the lattice parameters obtained in Section 3.1 guide our choice of initial coordinates and RF system parameters. We typically track nine particles, which define an area in longitudinal phase space, and yield an indication of the longitudinal acceptance of the FFAG ring. Longitudinally, the particles are injected into the ring at  $p_l < 0$  close to a zero crossing of the RF waveform, get accelerated across the peak of the RF waveform, and are

extracted from the ring at  $p_l > 0$  close to the neighbouring zero crossing of the RF waveform. Transversely, the particles are injected at or close to their respective closed orbit. The simulation of transverse motion with finite transverse emittances is beyond the scope of this paper. In Section 3.4.1, we study acceleration in ideal rings, without alignment errors. In Section 3.4.2, we include transverse alignment errors. All magnets are displaced individually with RMS displacements of 0.03 or 0.1 mm. The distributions of the displacements are Gaussians, truncated at 2.5 standard deviations.

#### 3.4.1. Rapid acceleration in ideal machines

Fig. 12 shows trajectories in longitudinal phase space for the Modified FODO lattice in Section

3.1. Nine particles are launched below the unstable fixed point at  $ct = 0.75 \pm 0.025$  m with  $pt = -0.68 \pm 0.01$ . The shape of the phase space trajectories in Fig. 12 is very similar to the contour plot of longitudinal phase space in Fig. 2. Such trajectories only occur when the peak accelerating voltage on the RF cavities  $V$  exceeds the threshold in Table 1, which can be calculated using Eq. (2), in fair agreement with the simulation that yields  $V = 1.45$  MV. Our typical RF voltage is about twice the threshold value. The normalised longitudinal phase space area occupied by the nine particles is about 0.15 m or 0.053 eV s, compared to 0.17 m in Ref. [10].

Fig. 13 shows the trajectories of nine particles in longitudinal phase space for the Doublet Lattice in Section 3.1. The particles start at  $ct = 0.75 \pm 0.025$  m with  $p_t = -1/3 \pm 0.02$ . All nine particles are accelerated along S-shaped trajectories, very similar to the contour plot of longitudinal phase space in Fig. 4, and reach their maximum momentum error  $p_t \approx 1/3$  above the stable fixed point at  $ct = -1.5$  m. The peak accelerating voltage on the RF cavities  $V = 13.5$  MV in the simulation is in good agreement with that calculated from Eq. (10),  $V = 13.3$  MV. The normalised longitudinal phase space area occupied by the nine particles is about 0.28 m or 0.1 eV s, compared to 0.17 m in Ref. [10].

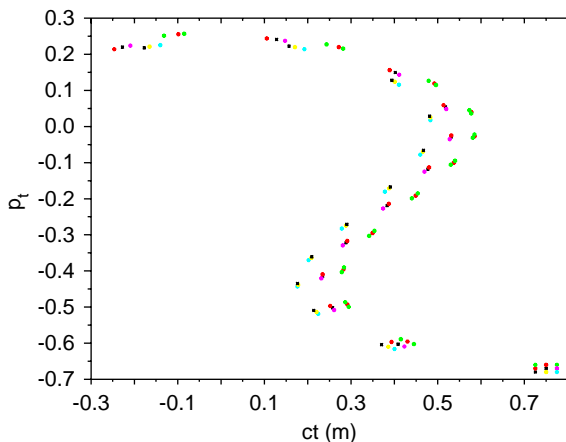


Fig. 12. Longitudinal phase space trajectories of nine particles, tracked for 11 turns, in the Modified FODO ring. The coordinates are recorded every turn.

A study of Figs. 12 and 13 shows that the distortion of longitudinal phase space is small and quite acceptable in the Doublet Lattice. The larger phase space distortions in the Modified FODO lattice require correction by a third harmonic RF system as has been demonstrated by Berg and Palmer [26].

### 3.4.2. Effects of misalignments on rapidly accelerated beams

In order to study the effects of misalignments on rapidly accelerated muon beams, we track nine muons in rings with misalignments, similar to what we did in Section 3.4.1. We launch the muons on the closed orbit in the ring without misalignments. Thus, we avoid the large orbit distortions, when the tunes at the initial momentum error  $\delta p/p$  are close to an integer, as discussed in Section 3.3. Figs. 14 and 15 show longitudinal phase space plots for two values of the RMS alignment errors, 0.03 and 0.1 mm, in the Modified FODO and Doublet Lattices, respectively. The left graph in Fig. 14 is very similar to Fig. 12, and shows that 0.03 mm RMS alignment errors are tolerable in the Modified FODO ring. The left and right graph in Fig. 14 are quite different. In the latter, several particles start on the wrong side of the separatrix, similar to the separatrices in Fig. 3 and are not accelerated. The left graph in Fig. 15 is very similar

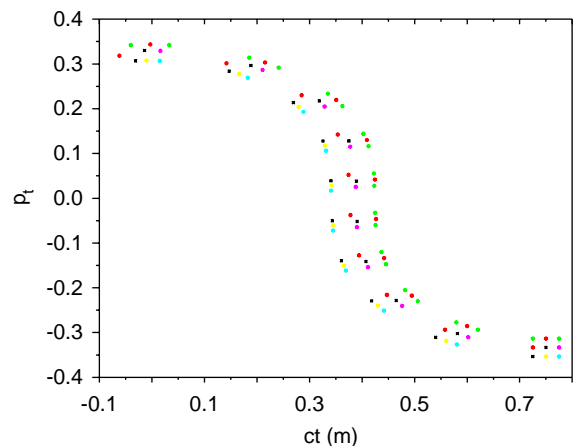


Fig. 13. Longitudinal phase space trajectory of nine particles, tracked for 9 turns, in the Doublet Lattice. The coordinates are recorded every turn.

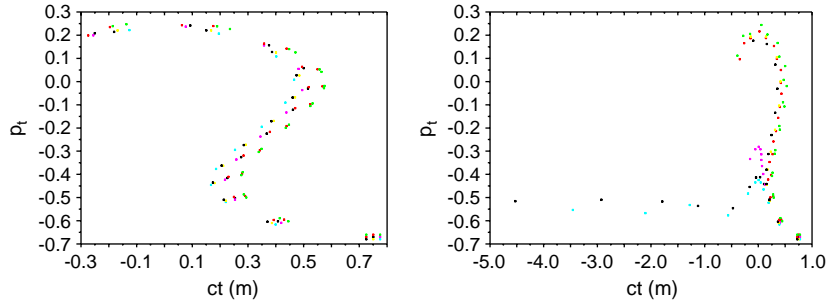


Fig. 14. Longitudinal phase space trajectories of nine particles, tracked for 11 turns, in the Modified FODO ring with misalignments. The RMS alignment errors are 0.03 mm in the left graph and 0.1 mm in the right graph. The coordinates are recorded every turn.

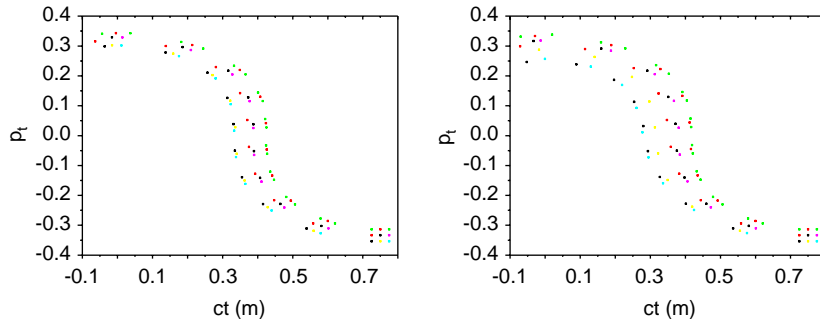


Fig. 15. Longitudinal phase space trajectories of nine particles, tracked for 11 turns, in the Doublet ring with misalignments. The RMS alignment errors are 0.03 mm in the left graph and 0.1 mm in the right graph. The coordinates are recorded every turn.

to Fig. 13, and shows that 0.03 mm RMS alignment errors are tolerable in the Doublet ring. The right graph in Fig. 15 shows a larger spread in the final particle coordinates than the left graph. If this emittance increase is to be avoided, the RMS alignment errors in the Doublet ring should be smaller than 0.1 mm.

#### 4. Electron model

An electron model with circumference and cost that, hopefully, are a few percent of those of an FFAG ring for muon acceleration would allow tests and demonstrations of the two critical issues, acceleration outside buckets and crossing of linear imperfection resonances. In this section we show that this goal can be realised.

##### 4.1. Electron model lattice

Table 2 shows the main parameters of the electron model lattice [15]. Compared to the lattice in Refs. [14,16], it is designed with longer horizontally focusing dipoles, in order to increase the ratio of their effective magnetic length and their aperture and to reduce their gradient. Also more space is provided between the dipoles in the triplet for the coils. The increased period length is compensated by increasing their number, in order to keep the path length variation approximately constant. Two horizontally focusing gradient dipoles surround a horizontally defocusing gradient dipole. The distance between the dipoles in the triplet is 40 mm. The combined-function dipoles are assumed to be rectangular magnets. Rectangular magnets have parallel end faces, and

Table 2  
Parameters of the electron model at 15 MeV reference energy

Number of cells	45
Cell length (m)	0.38
F magnet length (mm)	50
F magnet angle (mrad)	−37.459
F magnet gradient (T/m)	5.638
F magnet field (mT)	−37.464
D magnet length (mm)	100
D magnet angle (mrad)	214.545
D magnet gradient (T/m)	−4.746
D magnet field (mT)	107.285

the reference trajectory enters and leaves them at an angle. One would naively expect that increasing the number of periods from 33 in Refs. [14,16] to 45 would decrease the bending angles in the ratio  $33/45 = 11/15$ . Table 2 shows that both bending angles are reduced much more, in particular the reverse deflection in the F magnets. The reduction of the gradient in the F magnet is to be expected from the increase of its length. The increase in the spacing between the F and D magnets causes a further reduction in the gradients of both. The consequences of these changes will be discussed in Section 4.2. Fig. 16 shows the optical functions  $\sqrt{\beta_x}$ ,  $\sqrt{\beta_y}$ , and dispersion  $D_x$ . The RF cavity is at the maximum of  $D_x$ . Hence, it is possible that dangerous synchro-betatron resonances are excited which investigation is beyond this paper.

The gradients of the F and D dipoles are adjusted such that the phases advance by  $q_x = 0.233$  and  $q_y = 0.184$  in a lattice cell on the reference orbit at  $\delta p/p = 0$ . Here and in the following, we use  $q_x$  and  $q_y$  for the tunes of single cells, and  $Q_x$  and  $Q_y$  for the tunes in the whole ring. With these nominal tunes, the tunes  $q_x$  and  $q_y$  at the lower edge of the momentum range should remain well below the intrinsic half-integral stop band at  $q = 1/2$ . The bending angles in the F and D magnets are adjusted such that the flight time through a lattice cell is approximately independent of the relative momentum error to first order near  $\delta p/p = 0$ . All results are computed with MAD [22] although its correctness for relative momentum errors much larger than a few percent is questionable.

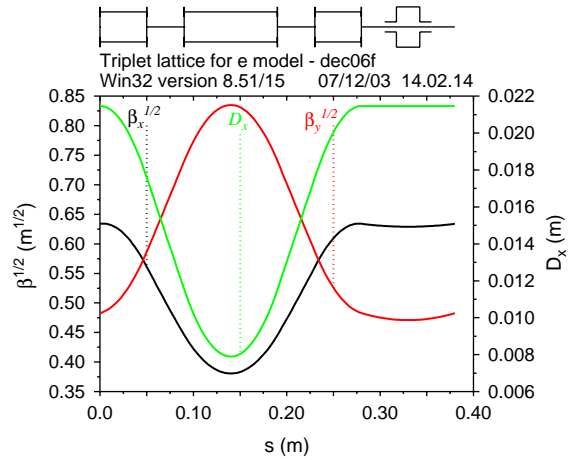


Fig. 16. Orbit functions in a cell of the electron model.

Fig. 17 shows the variation of the tunes  $q_x$  and  $q_y$  with the momentum error  $\delta p/p$  for a single lattice cell. The lower edge of the momentum range is caused by the vertical tune  $q_y$  approaching  $1/2$  from below. The upper edge of the momentum range is caused by the vertical tune  $q_y$  approaching  $0$  from above. The betatron oscillations are stable within the range  $-0.38 \leq \delta p/p \leq 0.69$ .

Fig. 17 shows the variation of the flight times with the momentum error  $\delta p/p$  for a single lattice cell, and gives the results for two different calculations, using the TWISS and TRACK commands in MAD [22], as discussed in Section 3.1. Both  $\delta(s)$  and  $ct$  vanish at  $\delta p/p = 0$ . The slope of  $ct$  at  $\delta p/p = 0$  is zero by design, while that of  $\delta(s)$  is almost zero. The leading variation of  $\delta(s)$  and  $ct$  with  $\delta p/p$  is quadratic. The spread in flight times is less than about  $0.73$  mm for  $-0.35 \leq \delta p/p \leq 0.35$ . For the whole ring with 45 cells, the spread in flight time is less than  $33$  mm. Fitting a parabola to  $ct$  in the neighbourhood of  $\delta p/p = 0$  yields the slip factor  $\eta_1$  listed in Table 5.

#### 4.2. Practical electron model lattice considerations

In order to compute the half apertures  $A_x$  and  $A_y$ , one needs the maxima of the absolute value of the orbit offset  $|x_c|$ , and of the  $\beta$ -functions  $\beta_x^{\max}$  and  $\beta_y^{\max}$  as functions of the relative momentum error  $\delta p/p$ , provided by MAD [22], as well as

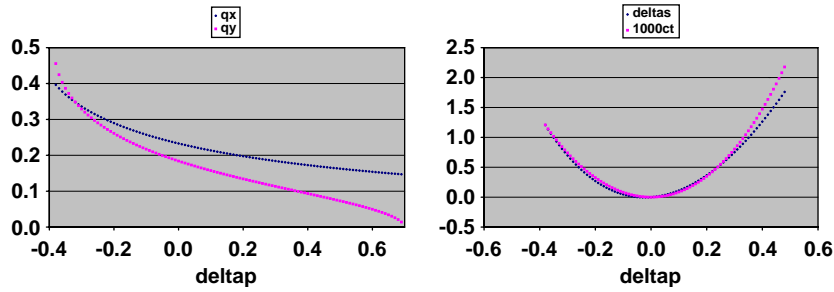


Fig. 17. Variation of the tunes  $q_x$  and  $q_y$  on the left, variation of orbit length  $\delta s$  and flight time  $ct$  in mm on the right, for a cell of the electron model with the relative momentum error  $\delta p/p$ .

parameters of the injected beam. Table 3 gives them for the ATF [27] at BNL, and the injector for CTF3 [28] at CERN. They are not necessarily optimised injectors for electron models of FFAG rings. To find the contribution of the betatron oscillations to the aperture, a normalised transverse RMS emittance  $\varepsilon_n = 0.3$  mm of the electron beam is assumed, and 3 RMS beam radii are allowed for in the half aperture. Here,  $\varepsilon_n$  is defined as the product of the RMS beam radius  $\sigma$  and RMS transverse momentum  $\Delta p/p_0$  in units of the electron rest momentum  $p_0$ . The figure  $\varepsilon_n = 0.3$  mm is the geometric mean between the figures in Table 3. In the horizontal plane, the betatron beam size is added to the orbit offset  $|x_c|$ . Fig. 18 shows the half apertures  $A_x$  and  $A_y$  thus obtained as functions of the relative momentum error  $\delta p/p$ . It may be seen that  $A_y \approx 10.7$  mm and  $A_x \approx 15.3$  mm are needed, for a momentum range  $-0.35 < \delta p/p < +0.35$ . This method of combining the maximum values of orbit offset  $|x_c|$  and  $\beta$ -functions  $\beta_x^{\max}$  and  $\beta_y^{\max}$  surely overestimates the vertical aperture  $A_y$  of the F magnets and the horizontal aperture  $A_x$  of the D magnets, and the magnetic field at the edge of the aperture in the D magnets.

Table 4 shows a summary of the field and aperture parameters of the electron model. The ratio of magnetic field and gradient  $B/G$  is the characteristic length, i.e. the lateral distance between the reference orbit and the radius where the magnetic field vanishes. Allowing a few mm for closed orbit distortions, in addition to the aperture radii shown in Fig. 18, yields the horizontal and

Table 3  
Typical parameters of electron beams

Parameter	ATF	CTF
Beam energy (MeV)	$\leq 72$	20
Normalised transverse emittance (rad m)	$10^{-3}$	$10^{-4}$
Normalised longitudinal emittance (eVs)	$2 \times 10^{-7}$	$10^{-6}$
Bunch charge (nC)	0.5	1

vertical aperture radii  $A_x$  and  $A_y$ , respectively. In the F magnets,  $B/G$  is smaller than the horizontal aperture radius  $A_x$ ; hence, they are assumed to be displaced quadrupoles, rather than C- or H-shaped gradient dipoles. In the D magnets,  $B/G \approx 22.6$  mm is larger than the horizontal aperture radius  $A_x$ ; hence, they are assumed to be half quadrupoles with a neutral pole. With respect to the centre of the quadrupole, where  $B = 0$ , the horizontal aperture is in the ranges of  $x$  shown in Table 4. Assuming that the hyperbolic pole face passes through the point with the largest value of  $x$  and  $y = A_y$ , yields the bore radius  $r$ . The pole tip field  $B(r)$  is obtained by using the gradients in Table 2. The current flowing around one pole in a steel-conductor quadrupole, in the absence of saturation, is  $I_m = rB(r)/2\mu_0$ , which formula is used in Table 4. The number of turns is a matter of magnet optimisation.

The pole tip field  $B(r)$  in Table 2 in the F magnets is a factor 3.2 smaller than in the earlier model [14]. In the D magnets,  $B(r)$  is still about 65% smaller. These pole tip fields are only a little higher than that achieved in the quadrupoles of the

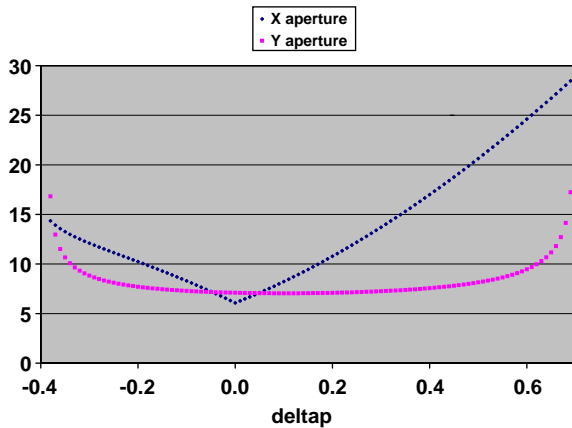


Fig. 18. Horizontal and vertical half apertures  $A_x$  and  $A_y$  of the electron model cell in mm as functions of the relative momentum error  $\delta p/p$ .

Table 4  
Field and aperture parameters of the electron model

	Magnet	
	F	D
$B/G$ (mm)	6.6	22.6
$A_x$ (mm)	$\pm 19$	$\pm 19$
$A_y$ (mm)	$\pm 12$	$\pm 12$
$x$ (mm)	$-12.4 \dots 25.6$	$3.6 \dots 41.6$
$r$ (mm)	24.8	31.6
$B(r)$ (T)	0.14	0.15
$I_m$ (A)	1381	1886

Recycler at Fermilab [30]. Permanent quadrupoles should be seriously considered. The maximum achievable  $B(r)$  should be investigated, and if needed, a small reduction in the accelerating range of the model should be foreseen, perhaps of the order of 10%.

#### 4.3. Misalignments

Fig. 19 shows the maxima of the absolute values of the horizontal and vertical orbit offset  $x_{co}^{\max}$  and  $y_{co}^{\max}$  due to the misalignment as a function of the horizontal tune  $Q_x$  and vertical tune  $Q_y$ , obtained as in Section 3.3. The spikes in  $x_{co}^{\max}$  and  $y_{co}^{\max}$  occur

when the corresponding tunes  $Q_x$  or  $Q_y$  are close to an integer. As in the earlier calculation [14] of an electron model with 33 cells, a standard deviation of 0.03 mm is adopted. The 45 triplets are assumed to be installed on girders that are displaced as a whole. The distribution of the displacements is a Gaussian, truncated at 2.5 standard deviations.

For the orbits of the reference particle at  $\delta p/p = 0$  due to the misalignment of the girders for 300 samples, we find  $\bar{x}_{co}^{\max} = 0.147 \pm 0.041$  mm and  $\bar{y}_{co}^{\max} = 0.266 \pm 0.083$  mm. Comparing these values to  $x_{co}^{\max} = 0.135$  mm and  $y_{co}^{\max} = 0.395$  mm for the ring used in Figs. 19 and 22 shows that it is close to the average behaviour horizontally, and pessimistic vertically.

For the maximum absolute values of horizontal dispersion  $D_x$  and vertical dispersion  $D_y$ , respectively, of the reference particle at  $\delta p/p = 0$  due to the misalignment of all girders as a whole for 300 samples we find  $\bar{D}_x = 23.5 \pm 0.732$  mm, compared to  $D_x = 21.5$  mm in the perfect ring, and  $\bar{D}_y = 8.93 \pm 4.20$  mm. Comparing these values to  $D_x = 23.8$  mm and  $D_y = 16.5$  mm for the ring used in Figs. 19 and 22 shows that it is close to the average behaviour horizontally, and pessimistic vertically.

In order to achieve the alignment tolerance assumed above, with a standard deviation of about 0.03 mm, the following steps are recommended: (i) The triplets are installed on girders. The three magnets on a girder are aligned on a measuring table to much better precision than 0.03 mm. (ii) The model ring is installed on a solid block of reinforced concrete that is isolated from the rest of the building. (iii) The vertical alignment is done with usual levelling techniques. (iv) The horizontal alignment is done by measuring the distance of the girders from the centre of the model, either by invar rods or by laser interferometry. Invar wires pulling at the girders are not recommended. (v) The support of the vacuum chamber and air pressure is independent from that of magnets and girders.

#### 4.4. Acceleration in the electron model

Table 5 shows the parameters of the RF system for the electron model, operated at two different

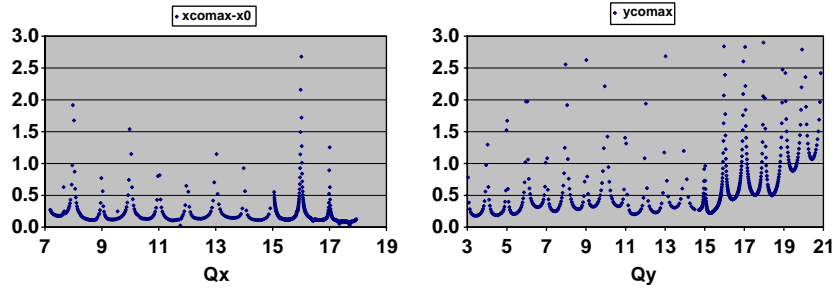


Fig. 19. Maxima of the absolute values of the horizontal and vertical orbit offset  $x_{\text{co}}^{\text{max}}$  and  $y_{\text{co}}^{\text{max}}$  in mm due to the misalignment as a function of the horizontal tune  $Q_x$  and vertical tune  $Q_y$ . The 45 triplets of the electron model are displaced as a whole.

choices of the accelerating voltages on the RF cavities: 20 and 50 kV. The accelerating range can be calculated from Eq. (10). It can also be found by tracking, adjusting the initial value of  $p_t$  such that the initial and final values of  $p_t$  have the same magnitude and opposite sign. The agreement between the analytical and tracking results is rather good.

The circumferential accelerating voltage, ranging from  $45 \times 20 \text{ kV} = 0.9 \text{ MV}$  to  $45 \times 50 \text{ kV} = 2.25 \text{ MV}$ , is a substantial fraction of the reference energy 15 MeV. Hence, the changes of  $p_t$  from turn to turn are substantial, as can be seen in Figs. 20 and 21. The number of turns needed to reach the final  $p_t$  is either 5 or 9 in the two examples. The similarity between the phase space plot in Fig. 4 and the trajectories in Figs. 20 and 21 is striking. The circumferential RF voltage  $N_c V$  in Eq. (10) is proportional to the cube of the accelerating range  $p_t$ , the harmonic number  $h$ , or the frequency  $f_{\text{RF}}$ , and the coefficient  $\eta_1$ , or the spread in flight times shown in Fig. 17. For given range  $p_t$ , the easiest way of reducing  $N_c V$ , or of making more efficient use of the RF system, and increasing the number of turns, is reducing  $h$  or  $\eta_1$ , or both.

#### 4.4.1. Longitudinal simulation in a perfect electron model

In Fig. 20, we launch nine electrons at  $ct = 50 \pm 2.5 \text{ mm}$  with  $p_t = -0.223 \pm 0.02$ , and track them for nine turns. They start on the closed orbit at the central value of  $p_t$ , and have no vertical and a small horizontal betatron amplitude. The nor-

Table 5

RF system parameters of the electron model for two accelerating voltages

RF cavity accel. voltage $V$ (kV)	20	50
Slip factor $\eta_1$	0.0149	0.0149
Number of cavities $N_c$	45	45
Harmonic number $h$	171	171
RF cavity power $P$ (W)	93.2	583
Stored energy $W_s$ (mJ)	0.0877	0.548
Range $p_t$ from (10)	0.224	0.304
Initial $p_t$	-0.2233	-0.3011
Final $p_t$	0.2234	0.3012
Number of turns $n$	9	5
Beam current $I_b$ (mA)	$\ll 8.5$	$\ll 21.4$

malised longitudinal phase space area enclosed is about 6 mm or  $10^{-5} \text{ eVs}$ . The electrons are accelerated, and reach their maximum  $p_t$  at  $ct = 0$ , those launched with lower  $p_t$  remain at lower  $p_t$ . The maximum acceleration is about 0.4 units of  $p_t$ , or from about 12 to about 18 MeV. More details are in the figure caption.

In Fig. 21, we launch nine electrons at  $ct = 50 \pm 2.5 \text{ mm}$  with  $p_t = -0.3 \pm 0.02$ , and track them for five turns. The range of acceleration increases from about 0.4 to about 0.5 units of  $p_t$ , when the accelerating voltage on the RF cavities is increased from 20 to 50 kV. This agrees with Eq. (10), which shows that increasing the RF voltage by a factor 2.5 increases the acceleration range by only a factor  $2.5^{1/3} \approx 1.36$ .

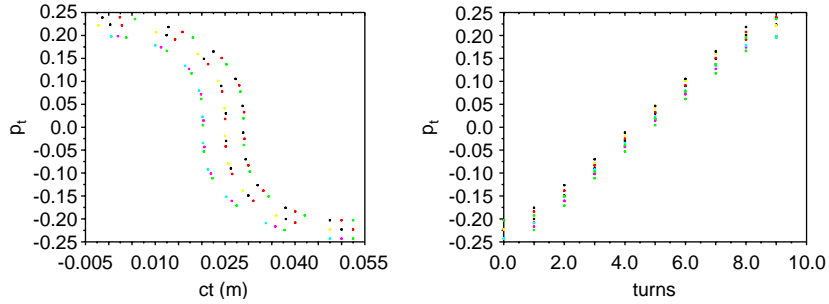


Fig. 20. Acceleration in the electron model with 0.9 MV peak circumferential RF voltage. Longitudinal phase space  $(ct, p_t)$  is on the left, the relative momentum error  $p_t$  vs. turns is on the right.  $V = 0$  at  $ct = -0.05, 0, +0.05$  m.  $V$  reaches the maximum at  $ct = 0.025$  m, and the minimum at  $ct = -0.025$  m.

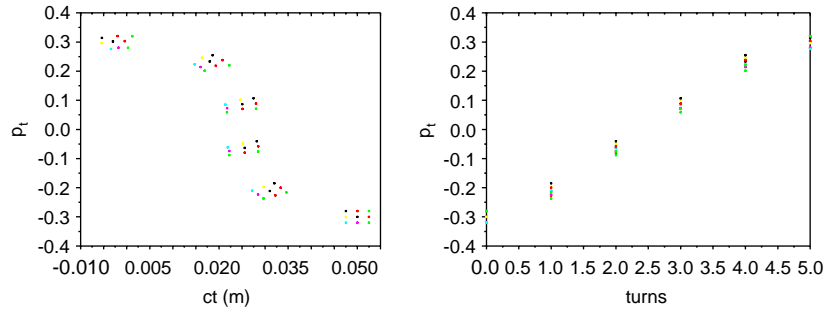


Fig. 21. Acceleration in the perfect electron model with 2.25 MV peak circumferential RF voltage without misalignments. Longitudinal phase space  $(ct, p_t)$  is on the left, the relative momentum error  $p_t$  vs. turns is on the right.

#### 4.4.2. Longitudinal simulation in an electron model with alignment errors

Fig. 22 shows the consequences of misalignments on the acceleration of the electrons. The triplets are installed on girders, which are displaced with 0.03 mm standard deviation, as in Fig. 19. The peak circumferential accelerating voltage is 2.25 MV as in Fig. 21. Comparing Figs. 21 and 22 show very similar behaviour, and suggests that the imperfection resonances can be crossed.

#### 4.5. Practical RF considerations for the electron model

We assume that an RF cavity is installed in each of the 45 lattice cells. The total circumferential voltage, 0.9 MV, corresponds to  $V = 20$  kV accel-

erating voltage in a cavity, or to 0.4 MV/m accelerating gradient. We assume that the RF cavities have the shape of a pillbox, are made of copper with conductivity  $\sigma = 5.8 \times 10^7 \Omega^{-1} \text{m}^{-1}$ , have intrinsic impedance  $R/Q = 121 \Omega$  and quality factor  $Q = 17733$ . We neglect the beam ports, and follow Ref. [29]. The RF power  $P$  needed in each RF cavity is

$$P = \frac{V^2}{2Q(R/Q)}. \quad (11)$$

Typical buncher cavities in S band linacs are very similar to the RF cavities envisaged here. All RF cavities can be fed from a single CW power source, probably a travelling wave tube, with a single waveguide around the circumference of the ring, equipped with couplers that tap off the

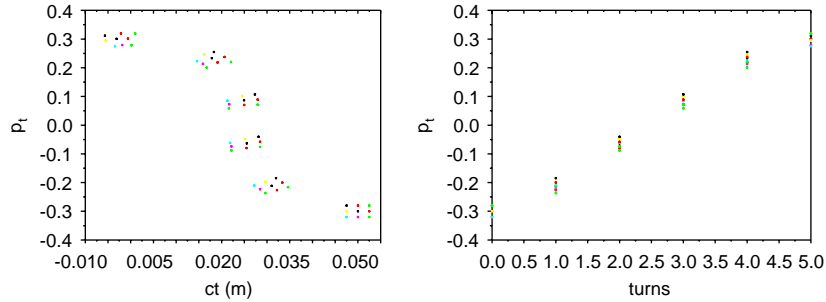


Fig. 22. Acceleration in the electron model with 2.25 MV peak circumferential RF voltage. The dipoles are installed on girders which are displaced with 0.03 mm standard deviation. Longitudinal phase space ( $ct, p_t$ ) is on the left, the relative momentum error  $p_t$  vs. turns is on the right.

appropriate amount of RF power at every RF cavity. Whether to install 45 RF cavities in all the longer straight sections, or only every so often, is related to the optimisation of the RF system and the space needed for other equipment, e.g. injection and ejection kickers.

#### 4.6. Beam loading

An estimate of beam loading of the RF cavities is obtained by comparing the energy extracted by the beam  $W_e$  to the stored energy  $W_s$  in the cavity, which is given by

$$W_s = \frac{V^2}{4\pi f_{\text{RF}}(R/Q)}. \quad (12)$$

Here  $f_{\text{RF}} \approx 3$  GHz is the frequency of the RF system. With beam current  $I_b$  and acceleration within  $n$  turns, the extracted energy  $W_e$  by the beam during all turns is

$$W_e = \frac{I_b C V n}{c\beta_r}. \quad (13)$$

Here,  $C$  is the circumference of the FFAG ring. Taking  $W_e/W_s \ll 1$ , yields an upper bound for the beam current  $I_b$ , displayed in Table 5:

$$I_b \ll \frac{V}{4\pi n h(R/Q)}. \quad (14)$$

Here,  $h$  is the harmonic number of the RF system. An accurate calculation of transient beam loading, taking into account the variation of phase and

acceleration shown in Fig. 21 is beyond the scope of this note. The beam observation system in the model must work to the expected accuracy at about the beam current  $I_b$  in Table 5.

## 5. Conclusions

In this paper, we concerned ourselves with the lattices and RF systems of FFAG rings for muon acceleration and, also, an FFAG electron model. We did not consider injection and extraction, diagnostics, and magnet design.

We have exhibited a Modified FODO lattice, with straight sections appropriate for a room-temperature RF system, which accelerates muons outside buckets from about 6 to about 20 GeV in about 10 turns with less than about 2 GeV circumferential acceleration  $V$ . This value of  $V$  is at most one half, and the number of arcs is 2/7, of those in an RLA with four turns, and there are no spreaders and combiners. The circumference  $C$  is  $\approx 1$  km. A Doublet Lattice is presented which is suitable for super-conducting RF and which also accelerates muon outside buckets from about 10 to about 20 GeV in 9 turns with 1.35 GV circumferential RF voltage, at  $C = 0.4$  km. The largest concern with these FFAG rings are the tight alignment tolerances required to cross resonances, which we find to depend on the lattice and fall into the range between 0.03 and 0.1 mm.

We have, also, derived parameters for the lattice and RF system of an electron model of a non-scaling FFAG ring, accelerating electrons from about 10–20 MeV. We have seen that such a model would allow one to explore the critical issues involved in the use of FFAGs. Spacings, magnet types and dimensions, and number of cells are presented. The model circumference is about 17 m, and the magnet half apertures are 10 mm × 20 mm. The number of periods in the model ring  $45 = 3^2 \times 5$  provides flexibility in the choice of the number of RF cavities, etc. The nominal tunes at  $\delta p/p = 0$ ,  $Q_x = 10.485$  and  $Q_y = 8.280$ , are well away from integral values. The pole-tip fields, about 0.15 T, are within the range of permanent-magnet quadrupoles [30]. The tune variation with momentum is similar to that in a full machine, and would allow the study of resonance crossing. The variation of orbit length with momentum is less than 35 mm, and would allow the study of acceleration outside a bucket. A 100 mm straight section, in each of 45 cells, is adequately long for an RF cavity operating at 3 GHz and of length half an RF wavelength. The accelerating voltage needed is calculated. Practical RF system design issues, e.g. RF power, and the limit on the bunch population due to beam loading are estimated.

## Acknowledgements

We like to thank the participants in the FFAG workshop at BNL in October 2003 for stimulating discussions, and R. Corsini, G. Geschonke, W. Kalbreier, M. Mayoud, L. Rinolfi and T. Zickler at CERN for helpful advice. The work of AMS was supported by the US Department of Energy under Contract No. DE-AC03-76SF00098.

## References

- [1] S. Machida, Nucl. Instr. and Meth. A 503 (2003) 41.
- [2] Y. Mori, J. Physics G 29 (2003) 1527.
- [3] C.J. Johnstone, S. Koscielniak, Recent progress on FFAGs for rapid acceleration, Proceedings of APS/DPF/DPB Summer Study on the Future of Particle Physics, Snowmass, 2001, p. T508.
- [4] D. Trbojevic, et al., Fixed field alternating gradient lattice design without opposite bend, Proceedings of EPAC, Paris, France, 2002, p. 1199.
- [5] C.J. Johnstone, S. Koscielniak, Recent progress on FFAGs for rapid acceleration, Proceedings of EPAC, Paris, France, 2002, p. 1261.
- [6] C. Johnstone, S. Koscielniak, Nucl. Instr. and Meth. A 503 (2003) 445.
- [7] E. Keil, A.M. Sessler, Muon acceleration in FFAG rings, Proceedings of PAC, Vancouver, Canada, 2003, p. 414.
- [8] D. Trbojevic, et al., FFAG lattice for muon acceleration with distributed RF, Proceedings of PAC, Vancouver, Canada, 2003, p. 1816.
- [9] N. Holtkamp, D. Finley (Eds.), A feasibility study of a neutrino source based on a muon storage ring, FERMI-LAB-PUB-00-108-E, 2000.
- [10] S. Ozaki, R. Palmer, M. Zisman, J. Gallardo (Eds.), Feasibility study II of a muon-based neutrino source, BNL-52623, June 2001, also at <http://www.cap.bnl.gov/mumu/studyii/FS2-report.html>.
- [11] P. Gruber, et al., The study of a European Neutrino Factory Complex, CERN-PS-2002-080-PP, 16 December 2002.
- [12] J.S. Berg, C. Johnstone, Design of FFAGs based on a FODO lattice, Proceedings of PAC, Vancouver, Canada, 2003, p. 2216.
- [13] J.S. Berg, et al., FFAGs for muon acceleration, Proceedings of PAC, Vancouver, Canada, 2003, p. 3413.
- [14] E. Keil, A.M. Sessler, An electron model of an FFAG muon accelerator, CERN-AB-2003-095 (AB) or CERN-NUFACT-Note-135, 2003.
- [15] E. Keil, Alternative electron models of an FFAG muon accelerator, AB-Note-2004-011 (ABP) or CERN-NUFACT-Note-137, 2004.
- [16] J.S. Berg, private communication.
- [17] J.S. Berg, Longitudinal reference particle motion in nearly-isochronous FFAG recirculating accelerators, Proceedings of APS/DPF/DPB Summer Study on the Future of Particle Physics, Snowmass, 2001, p. T503.
- [18] J.S. Berg, Dynamics in imperfectly-isochronous FFAG accelerators, Proceedings of EPAC, Paris, France, 2002, p. 1124.
- [19] S. Koscielniak, C. Johnstone, Longitudinal dynamics in an FFAG accelerator under conditions of rapid acceleration and fixed, high RF, Proceedings of PAC, Vancouver, Canada, 2003, p. 1831.
- [20] K.Y. Ng, in: A.W. Chao, M. Tigner (Eds.), Handbook of Accelerator Physics and Engineering, 2nd printing, World Scientific, Singapore, 2002, p. 94.
- [21] K.Y. Ng, Higher-order momentum compaction for a simplified FODO lattice and comparison with SYNCH, FERMI-LAB-FN-578, 1991, with errata in 1997.
- [22] H. Grote, F.C. Iselin, The MAD program, Version 8.16, User's Reference Manual, CERN SL/90-13 (AP) Rev.4, 1995.
- [23] A. Piwinski, Durch Störungen verursachte vertikale Dispersion, PETRA-Kurzmitteilung Nr. 79, 1976.

- [24] E. Keil, J. Kewisch, K. Steffen, H. Zygier, Comparative study of 100 GeV electron storage ring lattices regarding the effect of magnetic distortions, DESY-PET-77-04, 1977.
- [25] T. Suzuki, Vertical dispersion produced by random closed orbit distortions and sextupoles, PEP-259, 1977.
- [26] J.S. Berg, R.B. Palmer, Longitudinal acceptance, FFAF Workshop, TRIUMF, April 2004.
- [27] I. Ben-Zwi BNL, private communication, Dec 2003.
- [28] H. Braun, et al., An injector for the CLIC test facility (CTF3), Proceedings of 20th International Linac Conference, Monterey CA, 2000, p. 98.
- [29] W. Schnell, in: A.W. Chao, M. Tigner (Eds.), Handbook of Accelerator Physics and Engineering, 2nd printing, Singapore, 2002, p. 526.
- [30] E. Keil, Permanent-magnet quadrupoles for neutrino factories, CERN-SL/2000-006 (AP), 2000.